

**On-shot, high-intensity laser aberration measurements via ponderomotive electron ejection**A. E. Raymond<sup>1,\*</sup>, S. Ravichandran<sup>2,3</sup>, S.-W. Bahk<sup>1</sup>, A. Longman<sup>4</sup>, L. Roso<sup>5</sup>, R. Fedosejevs<sup>6</sup>, C. Mileham,<sup>1</sup>  
I. A. Begishev,<sup>1</sup> S. Qin<sup>1</sup>, N. Dauphin<sup>1</sup>, J. Shamlian<sup>1</sup>, W. T. Hill, III<sup>2,3,7</sup> and H. G. Rinderknecht<sup>1</sup><sup>1</sup>Laboratory for Laser Energetics, Rochester University, Rochester, New York 14623-1299, USA<sup>2</sup>Institute for Physical Science and Technology, University of Maryland, College Park, Maryland 20742, USA<sup>3</sup>Joint Quantum Institute, University of Maryland, College Park, Maryland 20742, USA<sup>4</sup>Lawrence Livermore National Laboratory, Livermore, California 94550, USA<sup>5</sup>Departamento de Física Aplicada, Universidad de Salamanca, 37008 Salamanca, Spain<sup>6</sup>Electrical and Computer Engineering, University of Alberta, Edmonton, Alberta T6G 2V4, Canada<sup>7</sup>Department of Physics, University of Maryland, College Park, Maryland 20742, USA

(Received 15 November 2024; accepted 13 January 2025; published 28 January 2025)

We present a technique to assess the spatial aberration content of a focused multiterawatt laser when fired at full power. This method leverages the direct detection of electrons ponderomotively accelerated from the focal volume formed in a low-pressure gaseous backfill. Our results show that the spatial distribution of emitted electrons exhibits distinct features correlated to the laser aberration type and magnitude. This work represents progress toward the complete and accurate *in situ* spatiotemporal characterization of focused high-intensity lasers.

DOI: [10.1103/PhysRevA.111.013121](https://doi.org/10.1103/PhysRevA.111.013121)**I. INTRODUCTION**

A focused laser can be described as *relativistic* when its intensity is sufficient to accelerate electrons to relativistic kinetic energies ( $\gtrsim 511$  keV) within one laser cycle. The characteristic intensity of a laser within its focal volume can be calculated from its energy, temporal duration, and focused spot size. For diffraction-limited Gaussian beams, this is expressed as  $I_0 = 2P/\pi\omega_0^2$ , where  $P$  is the peak laser power and  $\omega_0$  is the Gaussian laser beam waist. Lasers capable of reaching and exceeding relativistic intensities of  $10^{19}$  W/cm<sup>2</sup> (corresponding to field amplitudes of  $10^{12}$  V m<sup>-1</sup> and  $10^4$  T) are increasingly accessible to researchers [1].

A laser's focused intensity is also frequently expressed in terms of the associated normalized vector potential, which in practical units is expressed as  $a_0 \simeq 0.86\lambda_0$  ( $\mu\text{m}$ ) $\sqrt{I_0}$  ( $10^{18}$  W/cm<sup>2</sup>). Here,  $\lambda_0$  is the laser's central wavelength in microns and  $I_0$  is the laser's focused intensity in  $10^{18}$  W/cm<sup>2</sup>. A laser for which  $a_0 > 1$  indicates that ionized electrons will be energized beyond their rest mass energy. The characteristic temperature of the resulting free-electron population is estimated [2] as the maximum energy of the electrons oscillating in the field of incident laser:  $k_B T_e = (\gamma_t - 1)m_0c^2$ , where  $\gamma_t = 1 + a_0^2/2$  and  $m_0c^2$  is the rest mass energy of an electron.

Relativistically focused lasers find many applications such as in miniature particle accelerators [3], bright x-ray sources [4], investigations of quantum electrodynamics [5], and the pursuit of laser-driven fusion [6]. State-of-the-art laser systems are currently operating at the petawatt level [7] and a record focused intensity of the order  $10^{23}$  W/cm<sup>2</sup> was reported in 2021 [8]. In all applications, knowledge of the

focal-spot distribution is essential in the interpretation of experimental results. Departures from an ideal, diffraction-limited focal spot are introduced via a multitude of origins, both before focusing (such as from variations in the beam quality) and during final focusing (such as coma and astigmatism from an off-axis parabolic focusing mirror), necessitating careful measurements.

The same properties that make these lasers interesting for scientific study and critical for practical applications also create difficulty in quantitatively characterizing their focal quality (and hence, their intensity). These intensities exceed the damage threshold of optical materials by many orders of magnitude [9], preventing direct imaging of the focus using a microscope objective and/or camera sensor. Hence, conventional techniques for direct focal-spot characterization of relativistically intense lasers rely on imaging the low-energy output of the laser. While a widespread practice, this methodology can be misleading as full-power shots may result in a degraded focal-spot distribution due to the effects of thermal distortion of optical components. Another common method utilizes a sampled pickoff from the main beam, which is attenuated and imaged onto a wavefront sensor [10] or its focus imaged using a proxy focusing element. This method will not capture focal-spot variations induced by optical elements after the sampling element, such as the primary focusing optic itself (which is often the largest contributor to focal spot aberrations).

Here, a method for direct assessment of focal-spot aberrations such as coma and astigmatism at full power is presented, which instead utilizes the effect of ponderomotive acceleration of electrons freed within the focal volume from a rarefied background gas (Fig. 1). It has been shown theoretically [2,11] and experimentally [12] that a free electron is nominally forward-accelerated away from the laser focus with an angle  $\theta$  relative to the laser axis that is dependent upon the energy that

\*Contact author: [araymond@lle.rochester.edu](mailto:araymond@lle.rochester.edu)

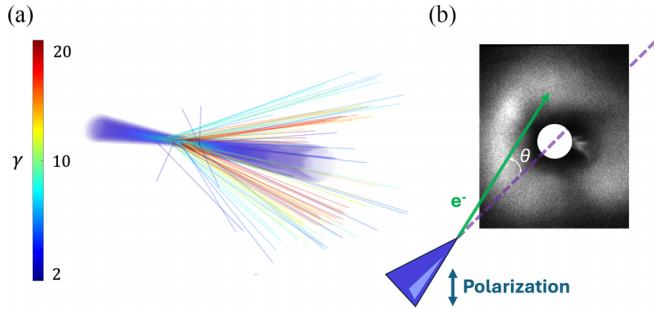


FIG. 1. Two perspectives of the interaction and detector geometry. (a) Simulation output of electrons (the outgoing paths of which are depicted) formed in and ejected from the laser focal volume, with more-energetic electrons (as parameterized by the Lorentz factor  $\gamma$ ) being more forward directed. The laser propagates from left to right in this image. (b) A 120 mm  $\times$  90 mm image plate is placed 25 mm beyond the laser focus, with a 20-mm-diameter hole for the laser to pass through. The image plate records the spatially resolved dose imparted by the electrons.

the electron gains from the laser, expressed via the Lorentz factor  $\gamma = (1 - v^2/c^2)^{-1/2}$ , where  $v$  is the electron's speed and  $c$  is the speed of light in vacuum. The peak value of  $\gamma$  may in turn be correlated with the local laser intensity [13,14]. Because focal aberrations lead to a nontrivial spatial distribution of laser intensity within the focal volume, each electron will exit the volume into a forward solid angle that correlates with the sampled intensity during its transit; thus, the global spatial distribution of exiting electrons carry a signature of the laser's aberration content.

In a recent work, indications of aberration content in such measured distributions were noted [14]. With the assumption of paraxially focused beams (focused with a large  $f_{\#} = f/D$  optic, where  $f$  is the focal length of the focusing optic and  $D$  is the incoming beam diameter), the effects of specific aberration content were predicted using simulations [13]. Short  $f_{\#}$  systems, however, are attractive for achieving the highest intensities, and paraxial approximation methods are invalid in this regime.

This paper presents experimental measurements of electron spatial distributions as the laser aberration content is controllably varied. In a short-focal-length configuration, coma and astigmatism were added to the beam using a programmable spatial light modulator (PSLIM) system [15]. Further, simulations in the short  $f_{\#}$  domain are presented, which aid in the interpretation of the data. The observation of distinctive, smoothly varying features in the resulting electron images suggest that a unique reconstruction of the focal spot is possible.

## II. BACKGROUND

It is known that in the presence of a paraxial, focused electromagnetic wave, electrons are forward-accelerated at an angle correlated to the energy they gain from the wave [11]:

$$\tan \theta = p_{\perp}/p_{\parallel} = \sqrt{2/(\gamma - 1)}, \quad (1)$$

where  $\gamma$  is the relativistic Lorentz factor introduced in the previous section and  $p_{\perp}$  ( $p_{\parallel}$ ) is the electron's momentum perpendicular (parallel) to the wave's propagation direction.

It has been computationally [2] and experimentally [12] shown that electrons ionized in a low-density gas in the presence of a focusing laser field will tend to follow this relation, with better agreement for paraxial (long  $f_{\#} \gtrsim 5$ ) focusing geometries in which plane-wave approximations can be applied to the focal volume of interest. From Eq. (1), it can be seen that a minimum cutoff angle  $\theta_{\min}$  would correlate with the highest energy imparted to electrons by the laser field. A suitable  $I(\gamma)$  relationship can then be used, as has been experimentally demonstrated for laser intensities of  $10^{19}$ – $10^{20}$  W/cm<sup>2</sup> with femtosecond-class lasers [13,14] and which appears extendable up to  $10^{21}$  W/cm<sup>2</sup> before the small  $\theta_{\min}$  complicates the intensity measurement.

With short focal lengths (corresponding to an  $f_{\#} \lesssim 5$ ), commonly used in high-intensity experiments, a large distribution of  $k$  vectors and a more prevalent longitudinal electric field lead to a deviation from the  $\gamma(\theta)$  relationship [16].

Ionization occurs when the focusing laser field sufficiently distorts the atomic potential barrier, reducing it to the ionization energy associated with a bound electron. Ionization energies for different atomic states are well documented [17], and various models can be applied to estimate the corresponding laser intensity. In barrier-suppression ionization [18], the appearance intensity at which an electron with ionization energy  $E_{\text{ion}}$  is ionized from the  $Z^{\text{th}}$  charge state can be approximated by the relation  $I_{\text{app}} = cE_{\text{ion}}^4/128\pi e^6 Z^2$ , where  $e$  is the elementary charge. For reference, the appearance intensities corresponding to the 18 electrons of the argon atom range from  $2.5 \times 10^{14}$  W/cm<sup>2</sup> for the outermost electron to  $5 \times 10^{21}$  W/cm<sup>2</sup> for the innermost electron. For the laser intensities used in this work, we expect to have ionized 16 of the 18 electrons available.

To systematically describe the aberrations, we utilize the convenient mathematical decomposition into the Zernike polynomial basis set on the unit disk [19]. This basis set explicitly describes common optical aberrations such as coma and astigmatism, which are the focus of this work. The Zernike polynomials utilized corresponded to (i) coma parallel to the laser polarization axis, (ii) coma perpendicular to this axis, and (iii) astigmatism applied at 45° to this axis. The polarity of the applied waveform aberrations was also varied.

To avoid collective or nonlinear plasma effects from complicating our analysis, the characteristic Debye length should be greater than the characteristic size of the focal region. For the laser parameters utilized in this experiment, the electron temperature is approximately  $k_B T_e \approx 1$  MeV. In this work, argon was used as the background fill gas. Conservatively assuming that all 18 electrons of the argon atoms are ionized, for the utilized background pressure of  $8.5 \times 10^{-4}$  Torr we calculate a Debye length of  $\lambda_D = \sqrt{\frac{\epsilon_0 k_B T_e}{e^2 n}} \approx 500$   $\mu\text{m}$ , where  $\epsilon_0$  is the electric permittivity of vacuum,  $e$  is the charge of an electron, and  $n$  is the volumetric density of electrons. The value of 500  $\mu\text{m}$  is much larger than the focal spot size of 10  $\mu\text{m}$ , justifying the neglect of collective effects.

## III. EXPERIMENTAL SETUP

The multiterawatt (MTW) laser [20] at the Laboratory for Laser Energetics is an optical parametric chirped pulse amplification system seeded at 1053 nm and amplified with

Nd:glass stages. The experiment described in this paper utilized the laser in a 10-J output mode with a full-width-at-half-maximum (FWHM) pulse duration of 700 fs, with 7.5 J transported to the final laser focus. The beam was apodized prior to final amplification to a circular tophat profile with a diameter of 70 mm. It was focused using an off-axis paraboloid (OAP) with a focal length of 200 mm, resulting in an  $f_{\#}$  of 2.8. An apochromatic microscope objective was used to image the resulting laser focus at low power and the OAP was adjusted to optimize the focal spot. The optimized focus exhibited mild horizontal elongation due to uncompensated wavefront tilt, resulting in an optimized focal spot area (at 75% intensity contour) of  $20 \mu\text{m}^2$  and a corresponding focused intensity of approximately  $I = 8 \times 10^{19} \text{ W/cm}^2$  (corresponding to  $a_0 \approx 8$ ).

Prior to final amplification and compression, the laser wavefront was manipulated using a PSLIM system, which was used to both optimize the wavefront for the nominal focus case as well as to controllably introduce wavefront aberrations. A series of aberration types and amplitudes were chosen for the experiment, including vertically ( $\parallel$  with polarization) and horizontally ( $\perp$  to polarization) directed coma, as well as oblique astigmatism ( $45^\circ$  to polarization, denoted “ $\angle$ ”) with amplitudes ranging in steps from  $-0.5\lambda$  to  $0.5\lambda$ , where  $\lambda$  is the laser central wavelength. A feedback optimization scheme was employed whereby the PSLIM settings were automatically adapted to generate the desired wavefront. The corresponding focal-spot microscope images were recorded at low energy under vacuum and are presented in Fig. 2.

A 120 mm  $\times$  90 mm Fujifilm BAS-MS image-plate (IP) detector with a 20-mm-diameter centered hole was utilized as the electron detector, covering a full cone angle of  $65^\circ$  from the laser focus. It was mounted consistently using a suspended mount 25 mm beyond the laser focus. The detector was shielded with 16- $\mu\text{m}$ -thick aluminum foil to prevent laser-induced signal or damage to the detector surface, and which blocked electrons with kinetic energies below approximately 40 keV from reaching the IP. The detector was exposed to a single shot before removing and scanning. The IP was scanned with a resolution of 50  $\mu\text{m}$  and the images were converted to units of photostimulated luminescence (PSL) using a published conversion formula [21].

Argon backfill into the target chamber was controlled using a pressurized needle valve assembly. The baseline chamber pressure was  $1 \times 10^{-5}$  Torr. Prior to each shot, the needle valve was manually opened until a steady, calibrated pressure of  $8.5 \times 10^{-4}$  Torr was indicated on the chamber pressure gauge.

As the aberration type and magnitude was varied, the spatial distribution of electrons varied as demonstrated in Fig. 2 along with the corresponding focal spot and (graphically embedded) nominal wavefront image. Concentrations of electron dose can be seen to gradually invert as the aberrated focal-spot distribution inverts in sign and magnitude, indicating that effects of the aberrations are transferred to the escaping electrons in a detectable and tractable manner.

#### IV. SIMULATIONS

To corroborate these results, a series of simulations was performed that captured the relevant aspects of the

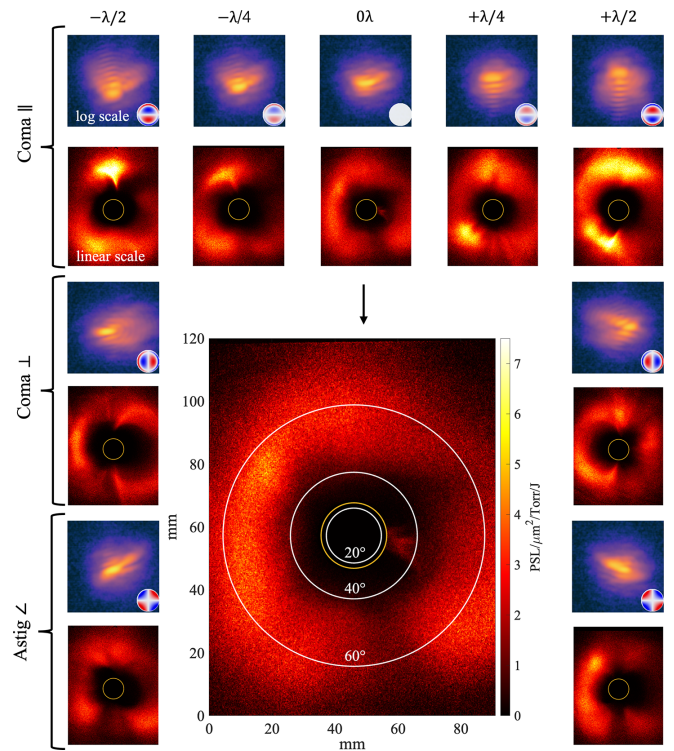


FIG. 2. A gallery of single-shot IP detector scans of the spatially resolved electron signal with corresponding low-energy focal spot images (logarithmic scale) is presented. The nominal focal spot case is enlarged and includes multiple  $\theta$  contours: the yellow contour represents the hole in the image plate; and the labeled white contours identify angles of  $20^\circ$ ,  $40^\circ$ , and  $60^\circ$  from the laser propagation axis. Attached to each focal spot image is a representation of the wavefront, with blue representing negative values, white representing zero, and red representing positive values.

experiment. The aberrated laser field was focused using a Stratton-Chu vector diffraction theory approach [22–24] to capture the effects of short  $f_{\#}$  focusing; within the focal volume, electrons were ionized from the defined gas species according to their tabulated ionization levels from a hybrid barrier suppression ionization (BSI) model [18,25] and the Ammosov-Delone-Krainov (ADK) tunneling ionization method [26]; and finally electron trajectories were calculated using a fourth-order Runge-Kutta computational solution to the Lorentz force equation. The simulation volume was defined as  $\pm 800 \mu\text{m}$  in the laser propagation axis and  $\pm 150 \mu\text{m}$  in the transverse axes, fully enclosing the region in which ionization occurs and in which electrons escape with ballistic trajectories.

We modeled the experimentally relevant MTW laser parameters in the simulation. For  $10^6$  iterations, a random plane perpendicular to the laser propagation direction was chosen; within this plane, a random point within the range of ionizing intensity was selected. The temporal evolution of the laser field was scanned at the selected point from a time long before the pulse arrives until the ionization occurred in order to determine the ionization time. Ionization was initiated when the field exceeded the BSI threshold corresponding to the current charge state. If the electric field intensity was below

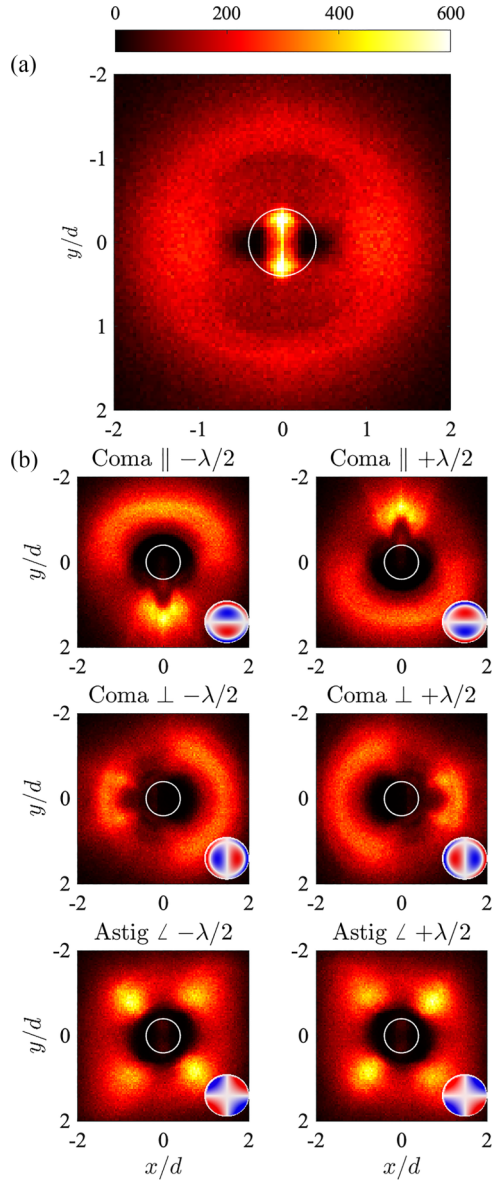


FIG. 3. The results of simulations performed are displayed in the form of 2D histograms of electron position as projected onto a plane beyond the laser focus. The axes are expressed as  $x/d$  and  $y/d$ , where  $x$  and  $y$  are the horizontal and vertical spatial axes respectively, and  $d$  is the distance of the plane from the center of focus. (a) The aberration-free case; the following are labeled according to their aberration type and magnitude as in Fig. 2. The white circle represents the extent of the diverging laser cone, and the color map corresponds to the number of data points within each grid cell. The laser is polarized in the vertical direction.

the threshold, then ionization was assessed based on tunneling ionization probability using a Monte Carlo ADK solver. Once ionization occurred, the freed electron was propagated in the time-varying laser fields until it intercepted an outer boundary. From the same initial ionization point, the atom continued to ionize to higher possible ionization states for the given local intensity.

In this way Fig. 3 was generated, in which the spatial distribution of ejected electrons are projected onto a plane

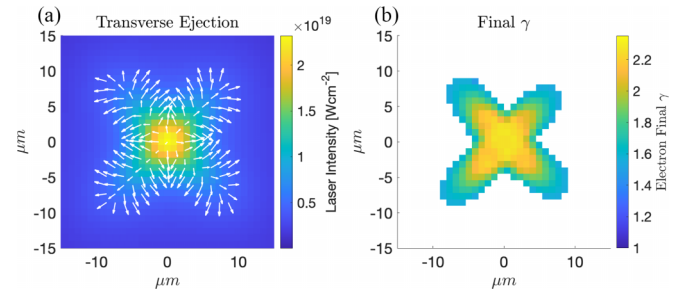


FIG. 4. (a) For the case of  $-\frac{1}{2}\lambda$   $\angle$  astigmatism, the laser intensity is shown averaged over  $800 \mu\text{m}$  in the propagation direction. Electrons are ionized within the focal volume (at the base of the depicted arrows) and ejected with at an angle with respect to this axis (in the direction of the arrowhead). In the transverse plane, they can be seen to eject in the direction of the falling gradient of laser intensity, consistent with the ponderomotive force. The white arrows represent the average ejection angle from within each grid cell. (b) The final average electron energies expressed in units of  $\gamma$ . Electrons born within a higher local laser intensity accumulate a higher resulting energy at the detector plane, and a correspondingly narrower forward angle as determined by Eq. (1). These dynamics combine to produce the resulting electron spatial distributions.

perpendicular to the laser propagation axis and presented as two-dimensional histograms; a series of experimentally relevant aberration types and magnitudes were scanned.

The simulations reproduce the trends observed in the experimental data. Inversion of the spatial distribution occur about the planes of symmetry observed in the laser waveforms as the polarity of the aberration is flipped. In the case of coma  $\parallel$ , a concentrated feature on the top or bottom is opposed by a broader feature on the opposite side in both the experimental and simulation data. In the astigmatism  $\angle$  case, an “X” pattern is evident in both experimental and simulation data. Some discrepancies are evident between the experimental and simulation data, which can be attributed to aberrations in the nominal experimental case that were not modeled in the simulation.

The electron spatial distributions can be interpreted by considering the local intensity profile of the focal spot: appreciable aberration leads to nontrivial structure in the intensity distribution. In the plane transverse to the laser propagation axis, electrons are ionized and ejected along the falling gradient of the local intensity (Fig. 4). Their forward velocity (and resulting forward angle of ejection) are determined by the energy gained as they escape the focal volume, nominally according to Eq. (1). An asymmetry is introduced by the polarization direction of the laser.

In the zero aberration case in Fig. 3, it is notable that two peaks exist in the electron spatial distribution within the white circle defining the diverging laser cone angle. A particle tracing analysis indicated that these electrons are ionized beyond best focus (as the laser is beginning to diverge) and become trapped within the laser cone due to the inward ponderomotive repulsion of electrons from the laser’s Airy diffraction ring structure. This effect is seen to discontinue when any appreciable aberration is added to the laser profile, so their presence may be a useful indicator of optimized focusing.

## V. CONCLUSIONS

In conclusion, we have demonstrated that for relativistically intense lasers in the short  $f_{\#}$  focusing regime, focal aberrations result in imprints upon the spatial distribution of electrons ponderomotively ejected from the focal volume. These imprints appear uniquely mapped, and vary gradually with changes in the aberration magnitude. Followup work will continue to assess the feasibility of using such measurements to reconstruct the focal-spot distribution using machine learning techniques, as well as to assess the applicability and limitations of the technique to femtosecond-class lasers. Particularly at the petawatt laser scale, these techniques become challenging to implement given the higher energy of accelerated electrons and the correspondingly smaller angle of ejection. Techniques to extend the range of applicability, such as the utilization of magnifying electron optics, are being considered as we further develop our simulation capabilities.

## ACKNOWLEDGMENTS

This material is based upon work supported by the Department of Energy (National Nuclear Security Adminis-

tration) University of Rochester “National Inertial Confinement Fusion Program” under Award No. DE-NA0004144, National Science Foundation Grants No. PHY2010392 and No. PHY2308905, the Natural Sciences and Engineering Research Council of Canada (RGPIN-2019-05013), and the U.S. Department of Energy by Lawrence Livermore National Laboratory under Contract No. DE-AC52-07NA27344.

This report was prepared as an account of work sponsored by an agency of the United States Government. Neither the United States Government nor any agency thereof, nor any of their employees, makes any warranty, express or implied, or assumes any legal liability or responsibility for the accuracy, completeness, or usefulness of any information, apparatus, product, or process disclosed, or represents that its use would not infringe privately owned rights. Reference herein to any specific commercial product, process, or service by trade name, trademark, manufacturer, or otherwise does not necessarily constitute or imply its endorsement, recommendation, or favoring by the United States Government or any agency thereof. The views and opinions of authors expressed herein do not necessarily state or reflect those of the United States Government or any agency thereof.

- 
- [1] R. Falcone, F. Albert, F. Beg, S. Glenzer, T. Ditmire, T. Spinka, and J. Zuegel, [arXiv:2002.09712](https://arxiv.org/abs/2002.09712).
  - [2] F. V. Hartemann, S. N. Fochs, G. P. Le Sage, N. C. Luhmann, J. G. Woodworth, M. D. Perry, Y. J. Chen, and A. K. Kerman, *Phys. Rev. E* **51**, 4833 (1995).
  - [3] T. Tajima and J. M. Dawson, *Phys. Rev. Lett.* **43**, 267 (1979).
  - [4] F. Albert, A. G. R. Thomas, S. P. D. Mangles, S. Banerjee, S. Corde, A. Flacco, M. Litos, D. Neely, J. Vieira, Z. Najmudin, R. Bingham, C. Joshi, and T. Katsouleas, *Plasma Phys. Controlled Fusion* **56**, 084015 (2014).
  - [5] P. Zhang, C. P. Ridgers, and A. G. R. Thomas, *New J. Phys.* **17**, 043051 (2015).
  - [6] M. Tabak, J. Hammer, M. E. Glinsky, W. L. Kruer, S. C. Wilks, J. Woodworth, E. M. Campbell, M. D. Perry, and R. J. Mason, *Phys. Plasmas* **1**, 1626 (1994).
  - [7] C. Radier, O. Chalus, M. Charbonneau, S. Thambirajah, G. Deschamps, S. David, J. Barbe, E. Etter, G. Matras, S. Ricaud *et al.*, *High Power Laser Sci. Eng.* **10**, e21 (2022).
  - [8] J. W. Yoon, Y. G. Kim, I. W. Choi, J. H. Sung, H. W. Lee, S. K. Lee, and C. H. Nam, *Optica* **8**, 630 (2021).
  - [9] A. A. Said, T. Xia, A. Dogariu, D. J. Hagan, M. J. Soileau, E. W. V. Stryland, and M. Mohebi, *Appl. Opt.* **34**, 3374 (1995).
  - [10] J. Bromage, S.-W. Bahk, D. Irwin, J. Kwiatkowski, A. Pruyne, M. Millecchia, M. Moore, and J. D. Zuegel, *Opt. Express* **16**, 16561 (2008).
  - [11] B. Quesnel and P. Mora, *Phys. Rev. E* **58**, 3719 (1998).
  - [12] C. I. Moore, J. P. Knauer, and D. D. Meyerhofer, *Phys. Rev. Lett.* **74**, 2439 (1995).
  - [13] A. Longman, S. Ravichandran, L. Manzo, C. Z. He, R. Lera, N. McLane, M. Huault, G. Tiscareno, D. Hanggi, P. Spingola, N. Czaplá, R. L. Daskalova, L. Roso, R. Fedosejevs, and W. T. Hill III, *Phys. Plasmas* **30**, 082110 (2023).
  - [14] S. Ravichandran, M. Huault, R. Lera, C. Z. He, A. Longman, R. Fedosejevs, L. Roso, and W. T. Hill III, *Phys. Rev. A* **108**, 053101 (2023).
  - [15] S.-W. Bahk, I. Begishev, and J. Zuegel, *Opt. Commun.* **333**, 45 (2014).
  - [16] A. Maltsev and T. Ditmire, *Phys. Rev. Lett.* **90**, 053002 (2003).
  - [17] A. Kramida, Yu. Ralchenko, J. Reader, and NIST ASD Team, NIST Atomic Spectra Database (ver. 5.12), National Institute of Standards and Technology, Gaithersburg, MD, 2025, <https://physics.nist.gov/asd>.
  - [18] S. Augst, D. Strickland, D. D. Meyerhofer, S. L. Chin, and J. H. Eberly, *Phys. Rev. Lett.* **63**, 2212 (1989).
  - [19] K. Niu and C. Tian, *J. Opt.* **24**, 123001 (2022).
  - [20] I. A. Begishev, V. Bagnoud, S.-W. Bahk, W. A. Bittle, G. Brent, R. Cuffney, C. Dorrer, D. H. Froula, D. Haberberger, C. Mileham, P. M. Nilson, A. V. Okishev, J. L. Shaw, M. J. Shoup, C. R. Stillman, C. Stoeckl, D. Turnbull, B. Wager, J. D. Zuegel, and J. Bromage, *Appl. Opt.* **60**, 11104 (2021).
  - [21] G. J. Williams, B. R. Maddox, H. Chen, S. Kojima, and M. Millecchia, *Rev. Sci. Instrum.* **85**, 11E604 (2014).
  - [22] S. W. Bahk, P. Rousseau, T. Planchon *et al.*, *Appl. Phys. B* **80**, 823 (2005).
  - [23] P. Varga and P. Török, *J. Opt. Soc. Am. A* **17**, 2081 (2000).
  - [24] J. Peatross, M. Berrondo, D. Smith, and M. Ware, *Opt. Express* **25**, 13990 (2017).
  - [25] S. Augst, D. D. Meyerhofer, D. Strickland, and S. L. Chin, *J. Opt. Soc. Am. B* **8**, 858 (1991).
  - [26] M. V. Ammosov, N. B. Delone, and V. P. Krainov, in *High Intensity Laser Processes*, Proceedings of SPIE Vol. 0664, edited by J. A. Alcock (SPIE, Bellingham, 1986), pp. 138–141.